J. Fluid Mech. (2013), *vol.* 720, *pp.* 545–557. © Cambridge University Press 2013
doi:10.1017/jfm.2013.50

Wake and thrust of an angularly reciprocating plate

Jeongsu Lee, Yong-Jai Park, Useok Jeong, Kyu-Jin Cho and Ho-Young Kim†

School of Mechanical and Aerospace Engineering, Seoul National University, Seoul 151-744, Korea

(Received 6 November 2012; revised 16 January 2013; accepted 18 January 2013;
first published online 27 February 2013)

As one of the most important force production mechanisms of swimming and flying animals, the fluid dynamics of flapping has been intensively studied. However, these efforts have been mainly directed toward animals in forward motion or locomotive appendages undergoing linear translation. Here we seek to complement the existing knowledge of the flapping mechanism by studying angularly reciprocating flat plates without a free stream velocity, under a so-called 'bollard pull' condition. We visualize the flow field around the flat plate to find that two independent vortical structures are formed per half-cycle, resulting in the separation of two distinct vortex pairs at sharp edges rather than a single vortex loop which is typical of a starting–stopping vortex paradigm in flows with free streams. Based on our observations, we derive a scaling law to predict the thrust of the flapping plate; this is the first experimentally validated theoretical model for the thrust of angularly reciprocating plates without a prescribed background flow.

Key words: biological fluid dynamics, propulsion, vortex flows

1. Introduction

Flapping is an essential mechanism for swimming and flying animals to produce lift and thrust. Thus, the force-generation mechanisms of various animals employing flapping, such as flying birds (Videler, Stamhuis & Povel 2004; Wu 2006, 2007), swimming fish (Lighthill 1970; Chopra 1976; Drucker & Lauder 1999) and hovering insects (Ellington *et al.* 1996; Dickinson, Lehmann & Sane 1999), have been studied intensely. An understanding of flapping also benefits the development of biorobots inspired by animal movement, such as flapping-based micro air vehicles (Zdunich *et al.* 2007) and robot fish (Yu *et al.* 2009). In general, such studies have focused on the cases where the animal is moving forward or the locomotive appendages translate linearly during flapping; the existence of a free stream plays an important role in these scenarios. The dynamics of vortices attached or bound to advancing foils are crucial in understanding the force-generation mechanism of lift-based propulsion systems, and thus a number of experimental (Birch & Dickinson 2003; Poelma, Dickson & Dickinson 2006; Buchholz & Smitz 2006, 2008; Jardin, David & Farcy 2009) and computational (Jones 2003; Dong, Mittal & Najjar 2006; Taira & Colonius 2009) studies have addressed the structure and temporal evolution of the vortices generated by flapping foils. However, the foregoing studies do not examine flapping foils without

† Email address for correspondence: hyk@snu.ac.kr

https://doi.org/10.1017/jfm.2013.50 Published online by Cambridge University Press

forward-propulsion properties and virtually non-existent free streams. This situation corresponds to the bollard pull condition of flapping (Newman 1977), which has been rarely considered, unlike its propeller-type propulsion counterpart (Kim & Chung 2006). Therefore, we seek to complement the existing knowledge of the flapping mechanism by studying angularly reciprocating flat plates in the absence of a free stream.

Investigations of flapping foils with virtually no free stream can also benefit the understanding of some biological movements such as the starting tail-fin motion of fish (Ahlborn *et al.* 1997), the drag-based propulsion of ducks (Kim & Gharib 2011) and the standing acrobatics of dolphins (Lang 1966). The flow field around a submerged plate that rotates from rest about a fixed axis has been visualized in previous studies (Ahlborn *et al.* 1997; Kim & Gharib 2011; DeVoria & Ringuette 2012). However, the thrust-generation mechanism of angular reciprocation of a fully immersed flat plate has not been treated thus far. The conventional theories for advancing foils cannot be directly applied to this case because flow separation behind the reciprocating plate is much more significant. In the following, we first describe an experimental apparatus that realizes the angular reciprocation of a rectangular flat plate and measures the thrust. We then present flow visualization results that unveil a hitherto unknown vortical structure that leads to a novel thrust-generation mechanism. On the basis of our observations, we derive a scaling law to predict the thrust of the angularly reciprocating flat plate as a function of the plate dimensions, stroke amplitude and frequency.

2. Experimental apparatus

Figure 1 shows an apparatus that visualizes the fluid flow and measures the resultant thrust simultaneously. A rectangular, rigid acrylic flat plate of 3 mm thickness is attached to a metallic rod of length $l = 12$ cm, which oscillates only about the z-axis. This single-degree-of-freedom motion is driven by a DC motor and a scotch-yoke mechanism. The stroke angle of the sinusoidal rotation $2\theta_m$ is fixed to 35°, and the frequency f ranges from 0.1 to 2.5 Hz. The width of the plate, w, was varied as 6, 8 and 12 cm, and its height, h, was varied as 4, 6 and 8 cm. The flat plate and rod assembly is immersed in a transparent water tank measuring 75, 55 and 33 cm in the x-, y- and z-directions, respectively, so that the free surface is 10 cm above the top of the flat plate. The Reynolds number, $Re = Uh/\nu$, defined based on the period-averaged, 0.7 radius length speed (Techet 2008), $U = 4(0.7R)\theta_m f$, ranges from 2.7×10^3 to 2.9×10^4. Here R is the radius of rotation of the plate tip, $R = h + l$, and ν is the kinematic viscosity of water. The normalized stroke amplitude $\beta = 2R\theta_m/h$ ranges from 1.5 to 4.6 and the aspect ratio $\eta = w/h$ ranges from 0.75 to 6.0. Platinum wires of 50 μm diameter are attached to the plate and connected to a power supply setup (Kenex HV-401) to generate hydrogen bubbles by the electrolysis of water. The central plane perpendicular to the plate is illuminated to visualize the bubbles with a 2 W continuous laser of 532 nm wavelength through a slit.

We employ two different techniques to visualize the flow using bubbles. First, by imaging bubbles with a high-speed camera (Photron APX-RS) at 60 frames per second (f.p.s.), the pathlines of the bubbles during the exposure time of 1/60 s are obtained. Second, the velocity field and vorticity contours are obtained by two-dimensional digital particle image velocimetry (DPIV). We use images of bubbles consisting of 600×673 pixels, captured at 125 fps. The movie is analysed by a DPIV software to generate a velocity field with 32×32 interrogation size and 50 % overlap. Derived

https://doi.org/10.1017/jfm.2013.50 Published online by Cambridge University Press

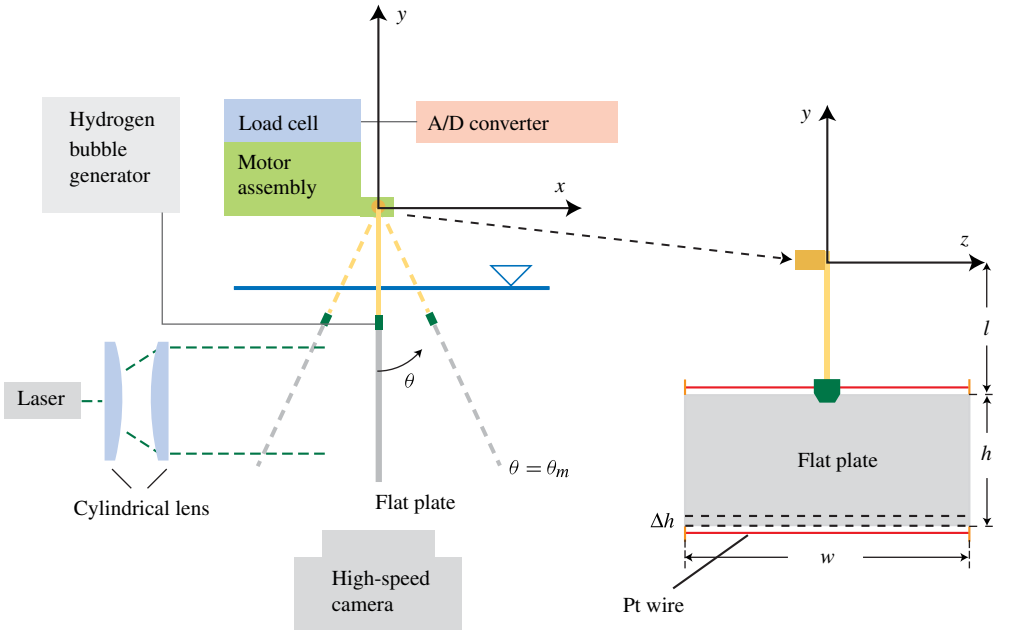


FIGURE 1. (Colour online) Experimental apparatus consisting of a flat plate oscillated about the z-axis immersed in a water tank, load cells, a hydrogen bubble generator, a laser and a high-speed camera. The front view of the flat plate shows a blade element in dashed lines, which is used in our modelling.

velocity vectors are validated by dynamic mean value operator. Error vectors are interpolated using a kriging interpolation. The number of error vectors is within 2 % of the total number of velocity vectors.

The thrust in the y-direction is measured by two force transducers (Ktoyo 333FB) at 2 kHz. The period-averaged thrust is obtained by averaging the sum of the measurement data of the force transducers over 10 periods of plate oscillation. We repeat the experiments three times and take the mean value of the period-averaged thrust results. All of the experiments were conducted after making sure that the oscillatory movement of the free surface had stopped to minimize the influence of the residual flow from previous experiments.

3. Flow visualization results

Figures 2 and 3 show the pathlines and vorticity contours, respectively, which visualize the fluid flows around the flat plate. While the pathlines of the bubbles visualize the newly generated vortices directly, the vorticity contours show the vortical structures shed away from the plate. These figures indicate that two distinct vortical structures arise per half cycle, hereafter termed as an acceleration-phase vortex (APV) and a stroke-reversal vortex (SRV). Figures 2(a) and 3(a) show the first vortical structure on the back face of the plate rotating counterclockwise toward the maximum stroke angle, θ_m. This vortex results from the plate acceleration occurring since the previous maximum stroke angle, $-\theta_m$, and thus is termed the APV. At θ_m, the second vortex rotating in the opposite sense to the existing APV is generated on the other side of the plate, as shown in figures 2(b) and 3(b), corresponding to the SRV. At

https://doi.org/10.1017/jfm.2013.50 Published online by Cambridge University Press

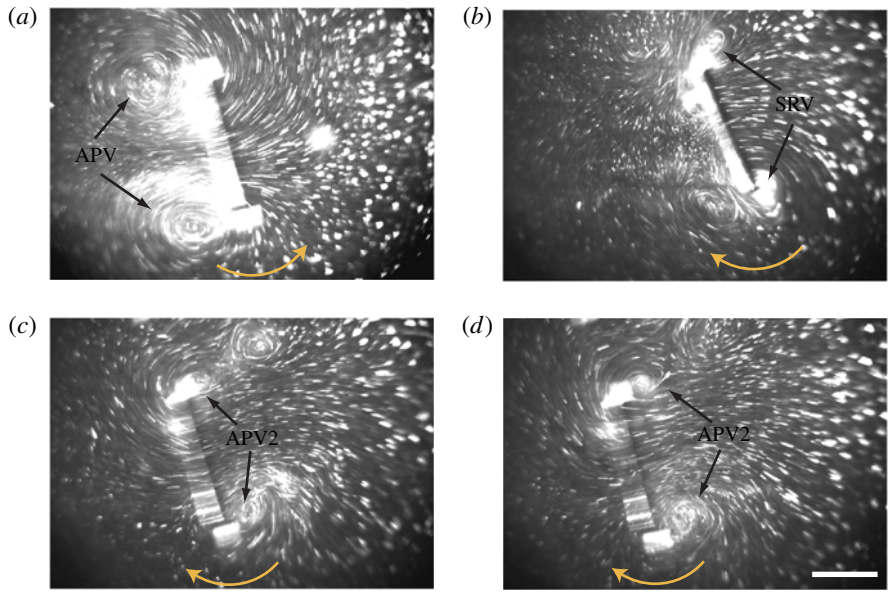


FIGURE 2. (Colour online) Visualization of flows via hydrogen bubbles around a flat-plate with $[h, w] = [4, 12]$ cm, oscillating at $f = 1.5$ Hz: (*a*) APV at $\theta = 10°$; (*b*) emergence of SRV at $\theta = 17°$; (*c*) emergence of APV at $\theta = 12°$; (*d*) reattachment of APV at $\theta = 5°$. The round arrow indicates the instantaneous direction of flat-plate rotation. Scale bar, 20 mm.

this moment, the APV and SRV coexist on the top and bottom edges of the plate, as clearly seen in figure 3(*b–c*). As the plate reaccelerates, as shown in figures 2(*c*) and 3(*c–d*), the APV and SRV are shed from the plate, forming vortex pairs. Figure 3 shows that the vortex pairs are shed at both the top and bottom edges. Also, another vortical structure emerges with the same rotational direction as the previous SRV: the APV of the clockwise half-cycle of plate oscillation (denoted as APV2 in figures 2 and 3). This vortex structure reattaches to the plate while the foregoing vortex pairs keep drifting away following self-induced currents, figure 2(*d*). Then, the flow pattern symmetrical to that of figure 3(*b*) is repeated at $-\theta_m$.

The observed flow characteristics are in stark contrast to those of the starting–stopping vortex in conventional aerodynamics (Newman 1977; Dickinson 1996). In the starting–stopping vortex paradigm, the starting vortex develops as the wing translation begins whereas the vorticity of equal strength but opposite sense is distributed along the wing surface. The resulting lift increases monotonically to the steady-state value from precisely half of the steady-state value (Newman 1977), which is referred to as the Wagner effect. The distributed vorticity separates as a stopping vortex at the end of the stroke, causing the loss of lift. The flow structure around flapping foils in natural situations can be explained by using the starting–stopping vortex paradigm (Drucker & Lauder 1999; Birch & Dickinson 2003; Buchholz & Smitz 2006; Dong *et al.* 2006; Poelma *et al.* 2006; Buchholz & Smitz 2008). We emphasize that while these starting and stopping vortices stem from a single vortex loop (Dickinson 1996), the angular reciprocation without a free stream forms two distinct vortical structures. As will be discussed below, the two force peaks occurring per half cycle, shown in figure 4, are then naturally correlated with the formation of the two vortical structures, APV and SRV.

https://doi.org/10.1017/jfm.2013.50 Published online by Cambridge University Press

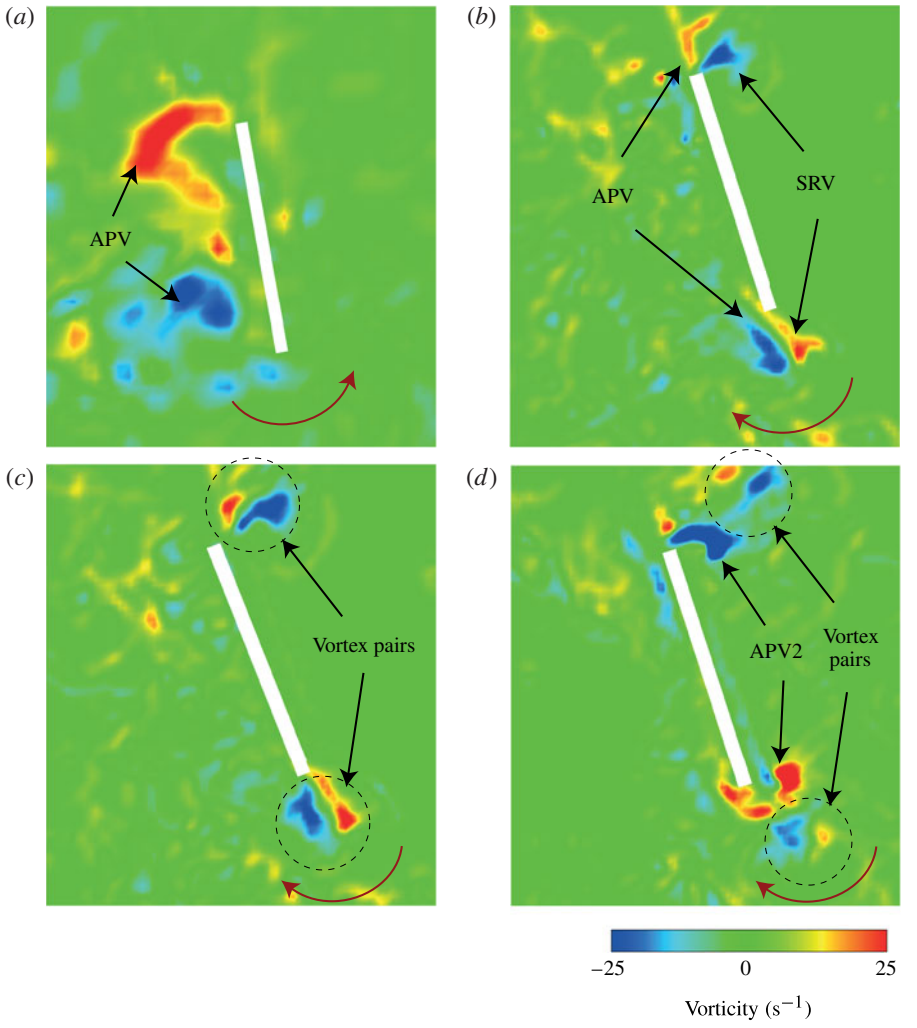


FIGURE 3. Vorticity contour around a flat-plate with $[h, w] = [4, 12]$ cm, oscillating at $f = 0.2$ Hz: (*a*) APV at $\theta = 10°$; (*b*) coexisting APV and SRV during stroke reversal at $\theta = 17°$; (*c*) shedding of two distinct vortex pairs around the top and bottom edges at $\theta = 15.5°$; (*d*) a newly generated APV during acceleration at $\theta = 14°$. The round arrow indicates the instantaneous direction of flat-plate rotation.

This marked change in vortex dynamics is mainly due to the difference in the angle of incidence of the fluid flow relative to the foil or plate motion. When a foil either moves forward or translates linearly between stroke reversals, the incident flow angle during flapping can be significantly reduced due to effective free stream velocities. However, the angularly reciprocating plate without a free stream faces the induced flow at an extremely high incident angle, near 90°. When the reciprocating plate reverses its direction, the flow following the plate cannot adjust itself smoothly to go around the plate. Instead, the flow separates at sharp edges due to the high incident angle, resulting in SRV. Previously reported flow fields around flapping foils with high angles of incidence are consistent with our observation. For the linearly reciprocating

https://doi.org/10.1017/jfm.2013.50 Published online by Cambridge University Press

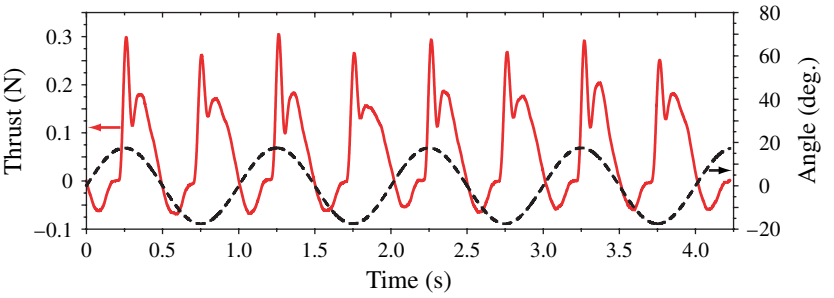


FIGURE 4. (Colour online) Experimentally measured thrust generated by a flat plate with $[h, w] = [4, 12]$ cm, oscillating at $f = 1$ Hz versus time.

foils corresponding to the angular reciprocation with an infinite radius, the shedding of vortex pairs at the top and bottom edges of a plate was clearly identified by the numerical computation of Jones (2003). Through experimental investigation of wake dynamics of a flapping foil imitating the wing motion of hovering insects, Jardin *et al.* (2009) found that two distinct vortex pairs, similar to the vortical structures reported in this work, arise at stroke reversal around both the leading and trailing edges when the angle of attack is higher than 45°. As the angle of attack decreases, the starting–stopping vortex behaviour was reported to occur at the stroke reversal. Similar tendency can be found in the computational results of Wang (2004) (figure 3 therein).

4. Scaling laws

On the basis of the flow visualization results, we construct a simple model to estimate the thrust. We start with dimensional analysis. The period-averaged thrust, $\langle F_t \rangle$, must be a function of fluid properties, plate dimensions, stroke frequency and amplitude, thus we write $\langle F_t \rangle = f(\rho, \mu, R, h, w, f, \theta_m)$. The Buckingham Π theorem (Buckingham 1914; Sonin 2004) allows us to write the following dimensionless relationship:

$$\frac{\langle F_t \rangle}{\rho h^4 f^2} = f\left(Re, \eta, \frac{R}{h}, \theta_m\right). \tag{4.1}$$

To go beyond this dimensional analysis, which lists only the dimensionless parameters determining the scaled thrust, and understand the force-production mechanism, we model the hydrodynamic forces acting on the angularly reciprocating plate. Two kinds of forces act on a flapping plate in general, one due to added mass and the other due to circulation. The force F_a due to added mass is generated as the plate velocity changes. For an angularly reciprocating plate whose angle is a sinusoidal function of time, the time mean of F_a over a period is zero because the added mass of a flapping plate in the rigid body motion can be assumed to be constant (Newman 1977). The vortical force, $\boldsymbol{F}_c$, is the time derivative of the vortical impulse, $\boldsymbol{I}$: $\boldsymbol{F}_c = \dot{\boldsymbol{I}}$. The mean force, $\langle \boldsymbol{F}_c \rangle$, which is of interest here, is scaled as

$$\langle \boldsymbol{F}_c \rangle = \frac{1}{T} \int_0^T \dot{\boldsymbol{I}} \, \mathrm{d}t \sim \frac{1}{T} \Delta \boldsymbol{I}, \tag{4.2}$$

https://doi.org/10.1017/jfm.2013.50 Published online by Cambridge University Press

where T is the period of flapping and $\Delta \boldsymbol{I}$ accounts for $\boldsymbol{I}$ produced by every new vortex structure within a cycle. In each cycle, two kinds of vortical structures are produced twice, i.e. two APVs and two SRVs are formed. Hence, we write

$$\Delta \boldsymbol{I} \sim 2(\boldsymbol{I}_A + \boldsymbol{I}_S), \tag{4.3}$$

where the subscripts A and S denote the APV and SRV, respectively.

The vortical impulse is determined by the distribution of vorticity in the flow field. Intense vorticity is distributed around the plate edge where the separation of vortical structures occurs. Thus, we can approximate the magnitude of the vortical impulse $\boldsymbol{I}$ using a vortex loop model: $I = \rho \Gamma wh$, where ρ is the density of water and Γ is the strength of the vortex loop. Then the magnitude of mean circulatory force, $\langle F_c \rangle$, is scaled as

$$\langle F_c \rangle \sim \rho whf(\Gamma_A + \Gamma_S). \tag{4.4}$$

Before proceeding to determine the magnitude of Γ we note that the circulation of the bottom edge is greater than that of the top edge due to a difference in linear acceleration. The Kelvin theorem dictates that vorticity is distributed over the plate surface to compensate for the difference in the circulation magnitudes at the edges. Hence, the total effective circulation induced by flapping can be scaled with the circulation at the bottom edge.

When a plate accelerates in a fluid, the pressure difference between the front and back faces is induced because the fluid must accelerate with the plate, which can be related to the acceleration of a virtual cylinder of fluid about the plate. This pressure difference cannot be maintained at the bottom edge and a vortical structure is then produced. By modelling the bottom edge as a blade element having a height Δh and width w as shown in figure 1, we get the added mass of the corresponding rectangular plate, $\sim \rho w^2 \Delta h$ (Newman 1977). Then, the added-mass force at the bottom edge is given by

$$F_a \sim \rho w^2 a \Delta h, \tag{4.5}$$

where the acceleration a is scaled as $a \sim Rf^2\theta_m$. Writing $F_a \sim \Delta p_a w \Delta h$, we get $\Delta p_a \sim \rho w R f^2 \theta_m$. Here Δh is considered small enough to ignore the variation of Δp_a along that length. The vortical structure that counterbalances this pressure difference can be modelled as a vortex sheet with tangential velocity discontinuity, ΔU_t, across the plate (Theodorsen 1935). Since Δp_a induces a vortical structure, we write $\Delta p_a \sim \rho \left(\Delta U_t\right)^2/2$. The vortex sheet should be shed tangentially to the plate (Wu, Ma & Zhou 2006) and evolved into a vortical structure, allowing us to write $\Delta U_t \sim \Gamma_i/h$. Therefore, we obtain the following scaling approximation of circulation:

$$\Gamma_i \sim hw^{1/2} R^{1/2} f \theta_m^{1/2}. \tag{4.6}$$

Because this procedure applies to both APV and SRV produced by sinusoidal reciprocation, i can be either A or S. The mean thrust for a period of flapping, $\langle F_t \rangle$, corresponding to $\langle F_c \rangle$, can be finally scaled as

$$\langle F_t \rangle \sim \rho h^2 w^{3/2} R^{1/2} f^2 \theta_m^{1/2}. \tag{4.7}$$

To validate our scaling analysis, we first measured the magnitude of circulation Γ experimentally. Limited by the power of the laser generator and the viewing area of the high-speed camera, we obtained vorticity fields for six cases with varying w (6, 8 and 12 cm), h (2, 4 and 6 cm) and f (0.1 and 0.2 Hz). Figure 5 shows the

https://doi.org/10.1017/jfm.2013.50 Published online by Cambridge University Press

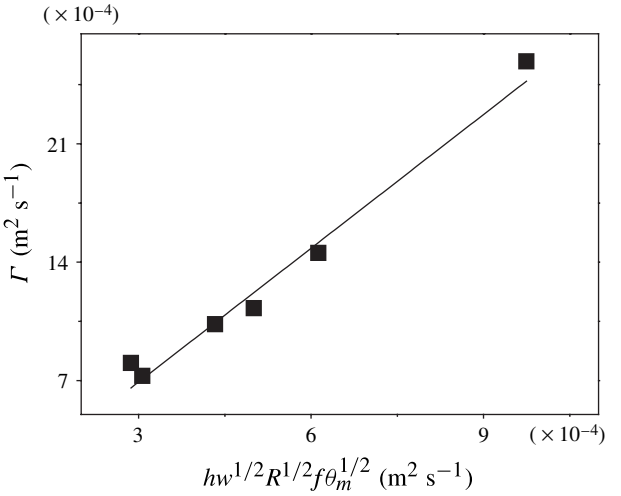


FIGURE 5. Measurement results of circulation plotted according to the scaling law, (4.6). The slope of the best-fitting line is 2.6.

measurement results of Γ at the bottom edge when the instantaneous θ is 16°. The circulation Γ was obtained by integrating the vorticity around the tail tip vortex. We see that Γ increases linearly with $hw^{1/2}R^{1/2}f$, consistent with our scaling law, (4.6), although θ_m is held constant in this work.

We now turn to the thrust, which could be measured across wide ranges of w, h and f. Figure 6 plots the mean thrust of 72 cases. Figure 6(a) shows that the mean thrust of a given geometry of plate increases linearly with f^2 while the data are scattered for differing h and w. All of the scattered data are collapsed onto a master curve when plotted according to the scaling law (4.7) as shown in figure 6(b). It is remarkable that our simple theory correctly captures the scaling relations of the period-averaged value of thrust, whose actual temporal evolution is by no means simple. This close agreement arises from the fact that the thrust is dominated by the impulsive generation of vortices (leading to the peaks in thrust), with which our theory is mainly concerned. Also, our simplification is supported by the fact that both added mass and the shape of vortical structures are determined by the plate geometry and that the plate rotation is sinusoidal.

The scaling law (4.7) can be rearranged so that the mean thrust scaled by $\rho h^4 f^2$ is expressed as a function of the normalized stroke amplitude $\beta = 2R\theta_m/h$ and the aspect ratio $\eta = w/h$:

$$\frac{\langle F_t \rangle}{\rho h^4 f^2} \sim \beta^{1/2}\eta^{3/2}, \tag{4.8}$$

where we dropped a numerical prefactor because the scaling relation is the principal interest. We see that our foregoing force analysis unveils the functional dependency of the scaled thrust on the dimensionless parameters which were merely listed in (4.1). Figure 7 replots the experimental data used in figure 6 according to (4.8), again validating our scaling law. Comparing the dimensionless relationship (4.1) and scaling law (4.8), it turns out that the scaled thrust is rather independent of Re in the range of Re tested in this work, i.e. 2.7×10^3–2.9×10^4. We suppose that it is because in

https://doi.org/10.1017/jfm.2013.50 Published online by Cambridge University Press

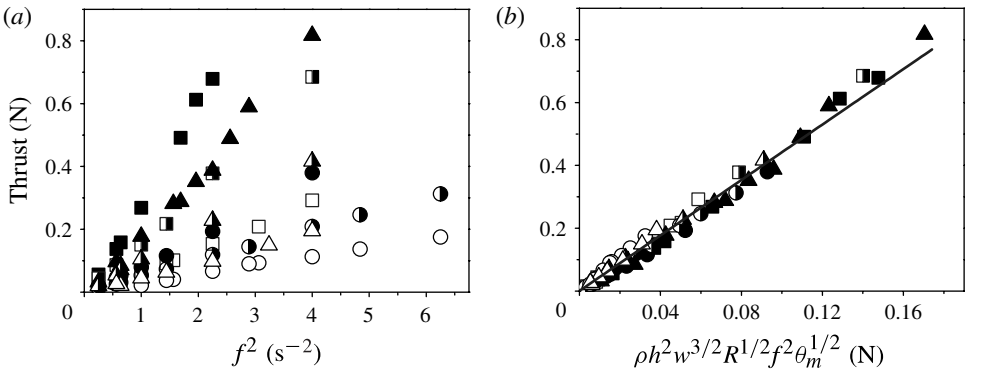


FIGURE 6. The mean value of period-averaged thrust, $\langle F_t \rangle$. (*a*) Plots of $\langle F_t \rangle$ versus f^2 for different plate geometries. The circles, triangles and squares correspond to the plates of $w = 6$, 9 and 12 cm, respectively. The empty, half-filled and filled symbols correspond to the plates of $h = 4$, 6 and 8 cm, respectively. (*b*) Plots of $\langle F_t \rangle$ plotted according to the scaling law (4.7). The straight line is drawn by the least-square method. The slope of the best-fitting line is 4.7.

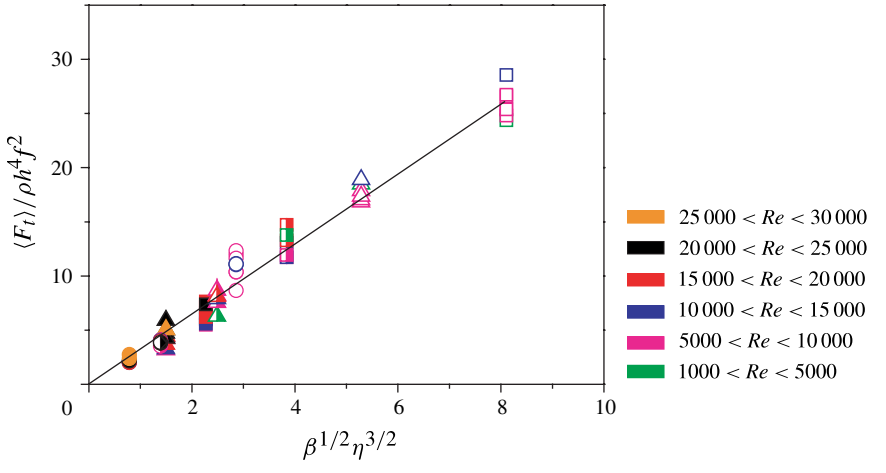


FIGURE 7. Dimensionless mean thrust, $\langle F_t \rangle / \rho h^4 f^2$, versus $\beta^{1/2} \eta^{3/2}$ for different plate geometries. The circles, triangles and squares correspond to the plates of $w = 6$, 9 and 12 cm, respectively. The empty, half-filled and filled symbols correspond to the plates of $h = 4$, 6 and 8 cm, respectively. Regardless of the Reynolds number varying between 2.7×10^3 and 2.9×10^4, the experimental data follow the scaling law (4.8). The slope of the best-fitting line is 3.3.

this range of *Re*, the ratio of convective to diffusive length scales is large enough to approximate the separating flow around the plate as a vortex sheet, a key assumption of the vortex topology in our model. The dimensionless parameters R/h and θ_m appear together as a product in β, a normalized stroke amplitude.

The bollard pull condition treated here is similar to having a Strouhal number, defined as $St = hf/\hat{U}$ based on forward velocity $\hat{U}$, of infinity. Thus, the comparison with previous studies on the behaviour of flapping foils at very large Strouhal numbers may provide further validation of our theory. However, the range of *St* investigated

https://doi.org/10.1017/jfm.2013.50 Published online by Cambridge University Press

thus far is rather limited mainly because most of flapping foils in natural situations work in a narrow range of St: $0.2 < St < 0.4$ (Taylor, Nudds & Thomas 2003). Among few studies that dealt with the cases where the flapping velocity is at least comparable to the forward propulsion velocity, Dong *et al.* (2006) provided detailed parameter values that allow the comparison of our theory with their results. As discussed in the appendix A, the comparison supports our scaling law favourably.

5. Conclusions

In summary, we have visualized vortex structures around a flapping plate undergoing angular reciprocation with no free stream, and measured the consequent thrust. In contrast to the conventional starting–stopping vortex behaviour, the angularly reciprocating plate was shown to generate two distinct vortical structures as it accelerates and reverses its direction due to a high angle of incidence between the plate and relative flow velocities. This topological difference in vortical structure affects the resulting force history. While the lift during the starting phase of the plate motion gradually increases in the starting–stopping vortex paradigm, an instantaneous force peak is induced when the plate accelerates in the angular reciprocation. In addition, the separation of the stopping vortex near the stroke reversal leads to a loss of lift in the starting–stopping vortex paradigm, whereas the SRV of angular reciprocation is believed to play a crucial role in force generation. The scaling law based on the assumption that the thrust production is dominated by the vortical impulses of APV and SRV was shown to agree well with the experimental measurements. We anticipate that the analysis of this canonical flapping configuration can greatly benefit the fundamental understanding of flapping fluid mechanics at high angles of incidence. It is worth further study to examine how the change in forward-propulsion velocity and consequent variation in incident flow angle influence the wake dynamics around the foil and the force history. Also, our theory for thrust generation can be a useful guideline for designing flapping-based biomimetic robots.

Acknowledgements

We are grateful to Professors L. Mahadevan and H. Choi for helpful discussions. This work was supported by Ministry of Education, Science and Technology (Converging Research Center Program grant No. 2012K001368) and National Research Foundation (grant No. 2011-0030744) of Korea through SNU-IAMD.

Appendix A. Comparison of the scaling law with high-St computational results

Dong *et al.* (2006) numerically computed the thrust coefficient C_T of foils flapping at high St, which varies as 0.6, 0.8, 1.0 and 1.2. At these high St, the incident flow angle is quite large near stroke reversals despite a relatively low angle of attack during linear translation (30° at the mid-line), which is expected to generate flow fields similar to those observed in this work. We convert their results as the following to compare with our scaling law (4.8). The expression for C_T can be rearranged to be related to $\langle F_t\rangle/(\rho h^4 f^2)$ as

$$\langle C_T\rangle = \frac{\langle F_t\rangle}{0.5\rho U^2 S} = \frac{2}{\pi}\frac{\langle F_t\rangle}{\rho h^4 f^2}\left(\frac{2Af}{\hat{U}}\right)^2\left(\frac{h}{A}\right)^2\frac{h}{w}, \tag{A 1}$$

https://doi.org/10.1017/jfm.2013.50 Published online by Cambridge University Press

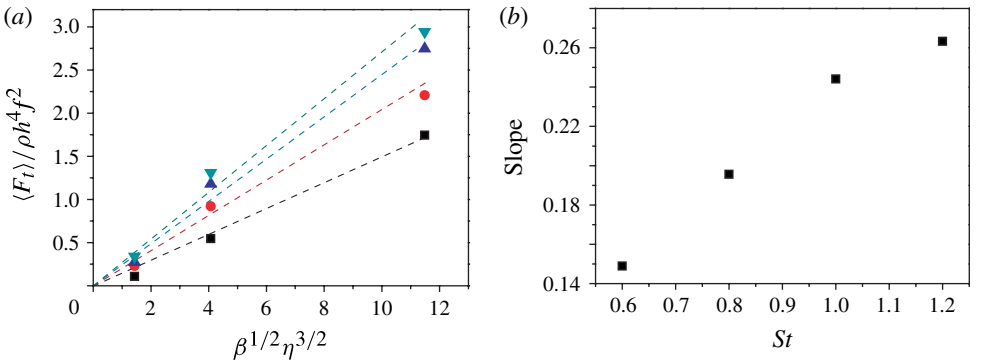


FIGURE 8. (Colour online) (*a*) Computational results of Dong *et al.* (2006) plotted according to the scaling law (4.8). The squares, circles, upright triangles and upside-down triangles correspond to $St = 0.6$, 0.8, 1.0 and 1.2, respectively. (*b*) The slope of best-fitting straight lines of (*a*) as a function of St.

Dong *et al.* (2006)			Converted data		
St	C_T	AR	β	η	$\langle F_t\rangle/(\rho h^4 f^2)$
0.6	0.1	1.27	1	1.27	0.109
0.6	0.25	2.55	1	2.55	0.546
0.6	0.4	5.09	1	5.09	1.744
0.8	0.375	1.27	1	1.27	0.230
0.8	0.75	2.55	1	2.55	0.921
0.8	0.9	5.09	1	5.09	2.208
1.0	0.7	1.27	1	1.27	0.274
1.0	1.5	2.55	1	2.55	1.180
1.0	1.75	5.09	1	5.09	2.747
1.2	1.25	1.27	1	1.27	0.340
1.2	2.4	2.55	1	2.55	1.311
1.2	2.7	5.09	1	5.09	2.943

TABLE 1. Raw data of Dong *et al.* (2006) and their converted values. Here $St = 2Af/U$ and AR is the aspect ratio.

where S is the foil area and A is the heave amplitude of the foil oscillation. Hence, the scaled thrust is written as

$$\frac{\langle F_t\rangle}{\rho h^4 f^2} = \frac{\pi}{2}\langle C_T\rangle\left(\frac{\hat{U}}{2Af}\right)^2\left(\frac{A}{h}\right)^2\frac{w}{h}. \tag{A 2}$$

Table 1 lists the values taken from Dong *et al.* (2006) and the derived quantities, β, η and $\langle F_t\rangle/(\rho h^4 f^2)$. We note that A/h was held constant at 0.5 in Dong *et al.* (2006). Plotting the data according to the scaling law (4.8), the scaled thrust indeed increases linearly with $\beta^{1/2}\eta^{3/2}$ at each St as shown in figure 8(*a*). The slope of the straight line increases with St as shown in figure 8(*b*). The difference of the slopes found in Dong *et al.* and the value predicted in our work, 3.3, is attributed to the small pitch-bias angle as well as the small St employed in Dong *et al.* (2006). Although further work

https://doi.org/10.1017/jfm.2013.50 Published online by Cambridge University Press

is necessary to fully confirm the consistency of these computational results and our scaling law (for example, the effects of *Re*, angle of attack, pitch-bias angle and non-dimensional stroke amplitude need to be investigated), the present comparison supports our scaling law favourably.

REFERENCES

AHLBORN, B., CHAPMAN, S., STAFFORD, R., BLAKE, R. W. & HARPER, D. G. 1997 Experimental simulation of the thrust phases of fast-start swimming of fish. *J. Exp. Biol.* **200**, 2301–2312.

BIRCH, J. M. & DICKINSON, M. H. 2003 The influence of wing-wake interactions on the production of aerodynamic forces in flapping flight. *J. Exp. Biol.* **206**, 2257–2272.

BUCHHOLZ, J. H. J. & SMITZ, A. J. 2006 On the evolution of the wake structure produced by a low-aspect-ratio pitching panel. *J. Fluid Mech.* **546**, 433–443.

BUCHHOLZ, J. H. J. & SMITZ, A. J. 2008 The wake structure and thrust performance of a rigid low-aspect-ratio pitching panel. *J. Fluid Mech.* **603**, 331–365.

BUCKINGHAM, E. 1914 On physically similar systems; illustrations of the use of dimensional equations. *Phys. Rev.* **4**, 345–376.

CHOPRA, M. G. 1976 Large amplitude lunate-tail theory of fish locomotion. *J. Fluid Mech.* **74**, 161–182.

DEVORIA, A. C. & RINGUETTE, M. J. 2012 Vortex formation and saturation for low-aspect-ratio rotating flat-plate fins. *Exp. Fluids* **52**, 441–462.

DICKINSON, M. H. 1996 Unsteady mechanisms of force generation in aquatic and aerial locomotion. *Am. Zool.* **36**, 537–554.

DICKINSON, M. H., LEHMANN, F.-O. & SANE, S. P. 1999 Wing rotation and the aerodynamic basis of insect flight. *Science* **284**, 1954–1960.

DONG, H., MITTAL, R. & NAJJAR, F. M. 2006 Wake topology and hydrodynamic performance of low-aspect-ratio flapping foils. *J. Fluid Mech.* **566**, 309–343.

DRUCKER, E. G. & LAUDER, G. V. 1999 Locomotor forces on a swimming fish: three-dimensional vortex wake dynamics quantified using digital particle image velocimetry. *J. Exp. Biol.* **202**, 2393–2412.

ELLINGTON, C. P., VAN DEN BERG, C., WILLMOTT, A. P. & THOMAS, A. L. R. 1996 Leading-edge vortices in insect flight. *Nature* **384**, 626–630.

JARDIN, T., DAVID, L. & FARCY, A. 2009 Characterization of vortical structures and loads based on time-resolved PIV for asymmetric hovering flapping flight. *Exp. Fluids* **46**, 847–857.

JONES, M. A. 2003 The separated flow of an inviscid fluid around a moving flat plate. *J. Fluid Mech.* **496**, 405–441.

KIM, J. & CHUNG, W. K. 2006 Accurate and practical thruster modelling for underwater vehicles. *Ocean Engng* **33**, 566–586.

KIM, D. & GHARIB, M. 2011 Characteristics of vortex formation and thrust performance in drag-based paddling propulsion. *J. Exp. Biol.* **214**, 2283–2291.

LANG, T. G. 1966 Hydrodynamic analysis of cetacean performance. In *Whales, Dolphins and Porpoises* (ed. K. S. Norris). University of California.

LIGHTHILL, M. J. 1970 Aquatic animal propulsion of high hydromechanical efficiency. *J. Fluid Mech.* **44**, 265–301.

NEWMAN, J. N. 1977 *Marine Hydrodynamics*. MIT.

POELMA, C., DICKSON, W. B. & DICKINSON, M. H. 2006 Time-resolved reconstruction of the full velocity field around a dynamically-scaled flapping wing. *Exp. Fluids* **41**, 213–225.

SONIN, A. A. 2004 A generalization of the Π-theorem and dimensional analysis. *Proc. Natl Acad. Sci. USA* **101**, 8525–8526.

TAIRA, K. & COLONIUS, T. 2009 Three-dimensional flows around low-aspect-ratio flat-plate wings at low Reynolds numbers. *J. Fluid Mech.* **623**, 187–207.

TAYLOR, G. K., NUDDS, R. L. & THOMAS, A. L. R. 2003 Flying and swimming animals cruise at a Strouhal number tuned for high power efficiency. *Nature* **425**, 707–711.

https://doi.org/10.1017/jfm.2013.50 Published online by Cambridge University Press

TECHET, A. H. 2008 Propulsive performance of biologically inspired flapping foils at high Reynolds numbers. *J. Exp. Biol.* **211**, 274–279.

THEODORSEN, T. 1935 General theory of aerodynamic instability and the mechanism of flutter. *NACA Report* 496.

VIDELER, J. J., STAMHUIS, E. J. & POVEL, G. D. E. 2004 Leading-edge vortex lifts swifts. *Science* **306**, 1960–1962.

WANG, Z. J. 2004 The role of drag in insect hovering. *J. Exp. Biol.* **207**, 4147–4155.

WU, T. Y. 2006 A nonlinear unsteady flexible wing theory. *Structural Control and Health Monitoring* **13**, 553–560.

WU, T. Y. 2007 A nonlinear theory for a flexible unsteady wing. *J. Engng Maths* **58**, 279–287.

WU, J.-Z., MA, H.-Y. & ZHOU, M.-D. 2006 *Vorticity and Vortex Dynamics*. Springer.

YU, J., HU, Y., HUO, J. & WANG, L. 2009 Dolphin-like propulsive mechanism based on an adjustable Scotch yoke. *Mechanism and Machine Theory* **44**, 603–614.

ZDUNICH, P., BILYK, D., MACMASTER, M., LOEWEN, D., DELAURIER, J., KORNBLUH, R., LOW, T., STANFORD, S. & HOLEMAN, D. 2007 Development and testing of the Mentor flapping-wing micro air vehicle. *J. Aircraft* **44**, 1701–1711.

https://doi.org/10.1017/jfm.2013.50 Published online by Cambridge University Press